Near-threshold neutral pion electroproduction at high momentum transfers and generalized form factors

P. Khetarpal,[30,12] P. Stoler,[30] I. G. Aznauryan,[35,40] V. Kubarovsky,[35,30] K. P. Adhikari,[29] D. Adikaram,[29] M. Aghasyan,[18] M. J. Amaryan,[29] M. D. Anderson,[37] S. Anefalos Pereira,[18] M. Anghinolfi,[19] H. Avakian,[35] H. Baghdasaryan,[38,29] J. Ball,[7] N. A. Baltzell,[1] M. Battaglieri,[19] V. Batourine,[35] I. Bedlinskiy,[22] A. S. Biselli,[11,5] J. Bono,[12] S. Boiarinov,[35,22] W. J. Briscoe,[15] W. K. Brooks,[36,35] V. D. Burkert,[35] D. S. Carman,[35] A. Celentano,[19] G. Charles,[7] P. L. Cole,[16,35] M. Contalbrigo,[17] V. Crede,[13] A. D'Angelo,[20,32] N. Dashyan,[40] R. De Vita,[19] E. De Sanctis,[18] A. Deur,[35] C. Djalali,[34] D. Doughty,[8,35] M. Dugger,[2] R. Dupre,[21] H. Egiyan,[35,39] A. El Alaoui,[1] L. El Fassi,[1] P. Eugenio,[13] G. Fedotov,[34,33] S. Fegan,[37] R. Fersch,[39,*] J. A. Fleming,[10] A. Fradi,[21] M. Y. Gabrielyan,[12] M. Garçon,[7] N. Gevorgyan,[40] G. P. Gilfoyle,[31] K. L. Giovanetti,[23] F. X. Girod,[35] J. T. Goetz,[28] W. Gohn,[9] E. Golovatch,[33] R. W. Gothe,[34] K. A. Griffioen,[39] B. Guegan,[21] M. Guidal,[21] L. Guo,[12,35] K. Hafidi,[1] H. Hakobyan,[36,40] C. Hanretty,[38] N. Harrison,[9] K. Hicks,[28] D. Ho,[5] M. Holtrop,[26] C. E. Hyde,[29] Y. Ilieva,[34,15] D. G. Ireland,[37] B. S. Ishkhanov,[33] E. L. Isupov,[33] H. S. Jo,[21] K. Joo,[9] D. Keller,[38] M. Khandaker,[27] A. Kim,[24] W. Kim,[24] F. J. Klein,[6] S. Koirala,[29] A. Kubarovsky,[30,33] S. V. Kuleshov,[36,22] N. D. Kvaltine,[38] S. Lewis,[37] K. Livingston,[37] H. Y. Lu,[5] I. J. D. MacGregor,[37] Y. Mao,[34] D. Martinez,[16] M. Mayer,[29] B. McKinnon,[37] C. A. Meyer,[5] T. Mineeva,[9] M. Mirazita,[18] V. Mokeev,[35,33,†] R. A. Montgomery,[37] H. Moutarde,[7] E. Munevar,[35] C. Munoz Camacho,[21] P. Nadel-Turonski,[35] R. Nasseripour,[23,12] S. Niccolai,[21,15] G. Niculescu,[23,28] I. Niculescu,[23] M. Osipenko,[19] A. I. Ostrovidov,[13] L. L. Pappalardo,[17] R. Paremuzyan,[40,‡] K. Park,[35,24] S. Park,[13] E. Pasyuk,[35,2] E. Phelps,[34] J. J. Phillips,[37] S. Pisano,[18] O. Pogorelko,[22] S. Pozdniakov,[22] J. W. Price,[3] S. Procureur,[7] D. Protopopescu,[37] A. J. R. Puckett,[35] B. A. Raue,[12,35] G. Ricco,[14,§] D. Rimal,[12] M. Ripani,[19] G. Rosner,[37] P. Rossi,[18] F. Sabatié,[7] M. S. Saini,[13] C. Salgado,[27] N. A. Saylor,[30] D. Schott,[15] R. A. Schumacher,[5] E. Seder,[9] H. Seraydaryan,[29] Y. G. Sharabian,[35] G. D. Smith,[37] D. I. Sober,[6] D. Sokhan,[21] S. S. Stepanyan,[24] S. Stepanyan,[35] I. I. Strakovsky,[15] S. Strauch,[34,15] M. Taiuti,[14,§] W. Tang,[28] C. E. Taylor,[16] S. Tkachenko,[38] M. Ungaro,[35,30] B. Vernarsky,[5] H. Voskanyan,[40] E. Voutier,[25] N. K. Walford,[6] L. B. Weinstein,[29] D. P. Weygand,[35] M. H. Wood,[4,34] N. Zachariou,[34] J. Zhang,[35] Z. W. Zhao,[38] and I. Zonta[20,‖]

(CLAS Collaboration)

[1]*Argonne National Laboratory, Argonne, Illinois 60439, USA*
[2]*Arizona State University, Tempe, Arizona 85287-1504, USA*
[3]*California State University, Dominguez Hills, Carson, California 90747, USA*
[4]*Canisius College, Buffalo, New York, USA*
[5]*Carnegie Mellon University, Pittsburgh, Pennsylvania 15213, USA*
[6]*Catholic University of America, Washington, DC 20064, USA*
[7]*CEA, Centre de Saclay, Irfu/Service de Physique Nucléaire, 91191 Gif-sur-Yvette, France*
[8]*Christopher Newport University, Newport News, Virginia 23606, USA*
[9]*University of Connecticut, Storrs, Connecticut 06269, USA*
[10]*Edinburgh University, Edinburgh EH9 3JZ, United Kingdom*
[11]*Fairfield University, Fairfield, Connecticut 06824, USA*
[12]*Florida International University, Miami, Florida 33199, USA*
[13]*Florida State University, Tallahassee, Florida 32306, USA*
[14]*Università di Genova, 16146 Genova, Italy*
[15]*The George Washington University, Washington, DC 20052, USA*
[16]*Idaho State University, Pocatello, Idaho 83209, USA*
[17]*INFN, Sezione di Ferrara, 44100 Ferrara, Italy*
[18]*INFN, Laboratori Nazionali di Frascati, 00044 Frascati, Italy*
[19]*INFN, Sezione di Genova, 16146 Genova, Italy*
[20]*INFN, Sezione di Roma Tor Vergata, 00133 Rome, Italy*
[21]*Institut de Physique Nucléaire ORSAY, Orsay, France*
[22]*Institute of Theoretical and Experimental Physics, Moscow, 117259, Russia*
[23]*James Madison University, Harrisonburg, Virginia 22807, USA*
[24]*Kyungpook National University, Daegu 702-701, Republic of Korea*
[25]*LPSC, Université Joseph Fourier, CNRS/IN2P3, INPG, Grenoble, France*
[26]*University of New Hampshire, Durham, New Hampshire 03824-3568, USA*
[27]*Norfolk State University, Norfolk, Virginia 23504, USA*
[28]*Ohio University, Athens, Ohio 45701, USA*
[29]*Old Dominion University, Norfolk, Virginia 23529, USA*
[30]*Rensselaer Polytechnic Institute, Troy, New York 12180-3590, USA*
[31]*University of Richmond, Richmond, Virginia 23173, USA*
[32]*Università di Roma Tor Vergata, 00133 Rome, Italy*
[33]*Skobeltsyn Nuclear Physics Institute, 119899 Moscow, Russia*

[34]*University of South Carolina, Columbia, South Carolina 29208, USA*
[35]*Thomas Jefferson National Accelerator Facility, Newport News, Virginia 23606, USA*
[36]*Universidad Técnica Federico Santa María, Casilla 110-V Valparaíso, Chile*
[37]*University of Glasgow, Glasgow G12 8QQ, United Kingdom*
[38]*University of Virginia, Charlottesville, Virginia 22901, USA*
[39]*College of William and Mary, Williamsburg, Virginia 23187-8795, USA*
[40]*Yerevan Physics Institute, 375036 Yerevan, Armenia*
(Received 28 November 2012; published 15 April 2013)

We report the measurement of near-threshold neutral pion electroproduction cross sections and the extraction of the associated structure functions on the proton in the kinematic range Q^2 from 2 to 4.5 GeV^2 and W from 1.08 to 1.16 GeV. These measurements allow us to access the dominant pion-nucleon s-wave multipoles E_{0+} and S_{0+} in the near-threshold region. In the light-cone sum-rule framework (LCSR), these multipoles are related to the generalized form factors $G_1^{\pi^0 p}(Q^2)$ and $G_2^{\pi^0 p}(Q^2)$. The data are compared to these generalized form factors and the results for $G_1^{\pi^0 p}(Q^2)$ are found to be in good agreement with the LCSR predictions, but the level of agreement with $G_2^{\pi^0 p}(Q^2)$ is poor.

DOI: 10.1103/PhysRevC.87.045205 PACS number(s): 25.30.Rw, 13.40.Gp, 14.20.Dh

I. INTRODUCTION

Pion photo- and electroproduction on the nucleon $\gamma N \to \pi N$, $\gamma^* N \to \pi N$ close to threshold has been studied extensively since the 1950s both experimentally and theoretically. Exact predictions for the threshold cross sections and the axial form factor were pioneered by Kroll and Ruderman in 1954 for photoproduction and are known as the low-energy theorem (LET) [1]. This LET provided model-independent predictions of cross sections for pion photoproduction in the threshold region by applying gauge and Lorentz invariance [2]. This was the first of the LET predictions to appear but was not without limitations. This LET predictions were restricted only to charged pions and the π^0 contribution was shown to vanish in the "soft pion" limit, i.e., $m_\pi \sim p_\pi$. Here, m_π and p_π are the mass and momentum of the pion. Additionally, these cross section predictions were limited to diagrams with first-order contributions in the pion-nucleon mass ratio. In later years, using vanishing pion mass chiral symmetry ($m_\pi \to 0$), these predictions were extended to pion electroproduction for both charged and neutral pions [3,4].

Of course, a vanishing pion mass does not relate to the observed mass of the pion (the pion to nucleon mass ratio $m_\pi/m_N \sim 1/7$), so higher order finite mass corrections to the LET were formulated in the late 1960s and early 1970s before the appearance of QCD. These also included contributions to the nonvanishing neutral pion amplitudes for the cross section.

In the late 1980s and early 1990s, experiments at Mainz [5] obtained threshold pion photoproduction data on $\gamma p \to \pi^0 p$. The theoretical predictions of LETs at the time were inconsistent with the data at low photon energies. With the emergence of chiral perturbation theory (χPT), the scattering amplitudes and some physical observables were systematically expanded in the low-energy limit in powers of pion mass and momentum. Using this framework, the LET was rederived to include contributions to the amplitudes from certain loop diagrams, which were lost when the expansion was performed in terms of the pion mass, as was done in the earlier works [6,7]. Further electroproduction experiments at NIKHEF [8] on $\gamma^* p \to \pi^0 p$ with photon virtuality $Q^2 \sim$ 0.05–0.1 GeV^2 [9] provided good agreement with χPT predictions.

These LETs [1,3,4,6,7] are not applicable for $Q^2 \gg \Lambda_{\rm QCD}^3/m_\pi$, where $\Lambda_{\rm QCD} \sim$ 200–300 MeV is the QCD scale parameter. In the case of asymptotically large momentum transfers ($Q^2 \to \infty$) perturbative QCD (pQCD) factorization techniques [10–12] have been used to obtain predictions for cross-section amplitudes and axial form factors near threshold. In these factorization techniques, "hard" ($Q^2 \gg \Lambda_{\rm QCD}^2$) and "soft" ($k \sim \Lambda_{\rm QCD}$) momentum contributions to the scattering amplitude can be separated cleanly and each contribution can be theoretically calculated using pQCD and LETs, respectively. Here, k is the momentum of the virtual photon.

Recently, Braun *et al.* [13,14] suggested a method to extract the generalized form factors, $G_1^{\pi N}(Q^2)$ and $G_2^{\pi N}(Q^2)$, for $1 < Q^2 < 10$ GeV^2 using light- cone sum rules (LCSRs). The transition matrix elements of the electromagnetic interaction, J_μ, can be written in terms of these form factors at threshold:

$$\langle N(P')\pi(k)|J_\mu|p(P)\rangle = -\frac{i}{f_\pi}\bar{N}\gamma_5\Big[(\gamma_\mu q^2 - q_\mu \not{q})\frac{G_1^{\pi N}(Q^2)}{m_N^2} - \frac{i\sigma_{\mu\nu}q^\nu}{2m_N}G_2^{\pi N}(Q^2)\Big]p. \quad (1)$$

Here, $N(P')$ and $p(P)$ are spinors for the final and initial nucleons with momenta P' and P, respectively, m_N is the mass of the nucleon, f_π is the pion decay constant, and q is the 4-momentum of the virtual photon. Because the pion

[*]Current address: Christopher Newport University, Newport News, Virginia 23606, USA.
[†]Current address: Skobeltsyn Nuclear Physics Institute, 119899 Moscow, Russia.
[‡]Current address: Institut de Physique Nucléaire ORSAY, Orsay, France.
[§]Current address: INFN, Sezione di Genova, 16146 Genova, Italy.
[‖]Current address: Università di Roma Tor Vergata, 00133 Rome, Italy.

is a negative-parity particle and the electromagnetic current is parity conserving, the γ_5 matrix is present to conserve the overall parity of the reaction.

These form factors are directly related to the pion-nucleon s-wave multipoles E_{0+} and L_{0+} [13,14]:

$$E_{0+} = \frac{\sqrt{4\pi\alpha}}{8\pi f_\pi}\sqrt{\frac{(2m_N+m_\pi)^2+Q^2}{m_N^3(m_N+m_\pi)^3}} \times\left(Q^2 G_1^{\pi N} - \frac{m_N m_\pi}{2} G_2^{\pi N}\right), \tag{2}$$

$$L_{0+} = \frac{\sqrt{4\pi\alpha}}{8\pi f_\pi}\frac{m_N|\omega_\gamma^{\rm th}|}{2}\sqrt{\frac{(2m_N+m_\pi)^2+Q^2}{m_N^3(m_N+m_\pi)^3}} \times\left(G_2^{\pi N} + \frac{2m_\pi}{m_N} G_1^{\pi N}\right). \tag{3}$$

Here, α is the electromagnetic coupling constant and $\omega_\gamma^{\rm th}$ is the virtual photon energy at threshold in the c.m. frame and is given by the following relation:

$$\omega_\gamma^{\rm th} = \frac{m_\pi(2m_N+m_\pi)-Q^2}{2(m_N+m_\pi)}. \tag{4}$$

In general, $E_{l\pm}$, $M_{l\pm}$, and $L_{l\pm}$ describe the electric, magnetic, and longitudinal multipoles, respectively. Here, l describes the total orbital angular momentum of the pion relative to the nucleon and $\pm$ is short for $\pm\frac{1}{2}$ so that the total angular momentum of the πN system is $l \pm \frac{1}{2}$.

Additionally, the sum rules can be extended to the $Q^2 \sim 1$ GeV^2 regime and the LETs are recovered to $O(m_\pi)$ accuracy by including contributions from semidisconnected pion-nucleon diagrams [14]. This approach provides a connection between the low and high Q^2 regimes. Predictions for the axial form factor and the generalized form factors are also obtained in this approach.

In the low $Q^2 < 1$ GeV^2 regime and the chiral limit $m_\pi \to 0$, the LET s-wave multipoles at threshold can be written as [7]

$$E_{0+} = \frac{\sqrt{4\pi\alpha}}{8\pi}\frac{Q^2\sqrt{Q^2+4m_N^2}}{m_N^3 f_\pi} G_1^{\pi N}, \tag{5}$$

$$L_{0+} = \frac{\sqrt{4\pi\alpha}}{32\pi}\frac{Q^2\sqrt{Q^2+4m_N^2}}{m_N^3 f_\pi} G_2^{\pi N}. \tag{6}$$

$G_1^{\pi N}$ and $G_2^{\pi N}$ can be written in terms of the electromagnetic form factors for the neutral pion-proton $\pi^0 p$ channel in this approximation:

$$\frac{Q^2}{m_N^2} G_1^{\pi^0 p} = \frac{g_A}{2}\frac{Q^2}{(Q^2+2m_N^2)} G_M^p, \tag{7}$$

$$G_2^{\pi^0 p} = \frac{2g_A m_N^2}{Q^2+2m_N^2} G_E^p. \tag{8}$$

In the above equations, G_M^p and G_E^p are the Sachs electromagnetic form factors of the proton and g_A is the axial coupling constant obtained from weak interactions. Also, for the charged pion-neutron $\pi^+ n$ channel, the generalized form factors can be written as

$$\frac{Q^2}{m_N^2} G_1^{\pi^+ n} = \frac{g_A}{\sqrt{2}}\frac{Q^2}{(Q^2+2m_N^2)} G_M^n + \frac{1}{\sqrt{2}} G_A, \tag{9}$$

$$G_2^{\pi^+ n} = \frac{2\sqrt{2} g_A m_N^2}{Q^2+2m_N^2} G_E^n. \tag{10}$$

Here, G_M^n and G_E^n are the electromagnetic form factors of the neutron. Additionally, G_A is the axial form factor that is induced by the charged current and its contribution comes from the Kroll-Ruderman term [1].

These generalized form factors, $G_1^{\pi N}$ and $G_2^{\pi N}$, can be described as overlap integrals of the nucleon and the pion-nucleon wave functions. The wave function of the pion-nucleon system at threshold is related to the nucleon wave function without the pion by a chiral rotation in the spin-isospin space [10,13]. The measurement of these form factors for pion electroproduction is, in essence, the measurement of the overlap integrals of the rotated and nonrotated nucleon wave functions, which are not accessible in elastic form factor measurements. This information complements our understanding of the various components of the nucleon wave function (quarks and gluons) and the theory of strong interactions. Additionally, it provides insight into chiral symmetry and its violation in reactions at increasing Q^2.

The generalized form factor for the charged pion-neutron $G_1^{\pi^+ n}(Q^2)$ and the axial form factor $G_A(Q^2)$ had been measured near threshold for $Q^2 \sim 2$–4.2 GeV^2 [15]. In this paper, we describe the measurement of the differential cross sections and the extraction of the s-wave amplitudes for the neutral pion electroproduction process, $ep \to ep\pi^0$, for $Q^2 \sim 2$–4.5 GeV^2 near threshold, i.e., $W \sim 1.08$–1.16 GeV. From these cross sections, the generalized form factors $G_1^{\pi^0 p}(Q^2)$ and $G_2^{\pi^0 p}(Q^2)$ were extracted and compared with the theoretical calculations of Refs. [7,14].

II. KINEMATIC DEFINITIONS AND NOTATIONS

The neutral pion reaction

$$e(l) + p(P) \to e(l') + p(P') + \pi^0(k) \tag{11}$$

is shown schematically in the virtual photon-proton c.m. frame in Fig. 1. Here, $l = (E_e, \mathbf{p_e})$, $l' = (E'_e, \mathbf{p'_e})$, $P = (m_p, \mathbf{0})$, and $P' = (E'_p, \mathbf{p'_p})$ are the initial and final electron and proton 4-momenta in the laboratory frame and $k = (E_\pi, \mathbf{p}_\pi)$ is the

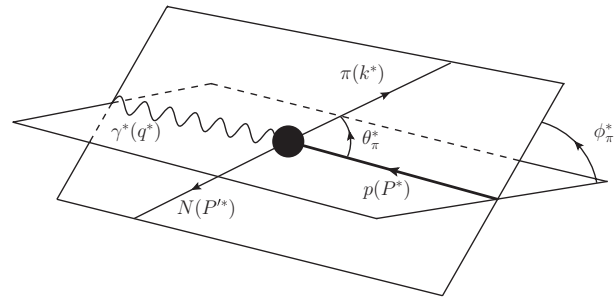

FIG. 1. Neutral pion electroproduction in the c.m. frame.

4-momentum of the emitted pion. Also, m_p refers to the mass of the proton. It is assumed that the incident electron interacts with the target proton via exchange of a single virtual photon with 4-momentum $q = l - l' = (\omega, \mathbf{q})$. In this approximation, it is also assumed that the electron mass is negligible ($m_e \approx 0$). The two important kinematic invariants of interest are

$$\begin{aligned} Q^2 \equiv -q^2 &= -\omega^2 + |\mathbf{q}|^2 = 4E_e E'_e \sin^2(\theta'_e/2), \\ s = W^2 &= (q + P)^2 = m_p^2 + 2\omega m_p - Q^2. \end{aligned} \tag{12}$$

Here, θ'_e is the polar angle of the scattered electron in the laboratory frame.

The fivefold differential cross section for the reaction can be written in terms of the cross section for the subprocess $\gamma^* p \to p\pi^0$ [16], which depends only on the matrix elements of the hadronic interaction:

$$\frac{d^5\sigma}{dE'_e d\Omega'_e d\Omega^*_\pi} = \Gamma \frac{d^2\sigma_{\gamma^* p}}{d\Omega^*_\pi}. \tag{13}$$

Here, $d\Omega'_e = d\cos\theta'_e d\phi'_e$ is the differential solid angle for the scattered electron in the laboratory frame and $d\Omega^*_\pi = d\cos\theta^*_\pi d\phi^*_\pi$ is the differential solid angle for the pion in the virtual photon-proton ($\gamma^* p$) c.m. frame. The azimuthal angle ϕ^*_π is determined with respect to the plane defined by the incident and scattered lepton [2]. The factor Γ represents the *virtual photon flux*. In the Hand convention [16] it is

$$\Gamma = \frac{\alpha}{2\pi^2} \frac{E'_e}{E_e} \frac{W^2 - m_p^2}{2m_p Q^2} \frac{1}{1-\varepsilon}, \tag{14}$$

which depends entirely on the matrix elements of the leptonic interaction and contains the *transverse polarization* of the virtual photon,

$$\varepsilon = \left(1 + 2\frac{|\mathbf{q}|^2}{Q^2} \tan^2 \frac{\theta'_e}{2}\right)^{-1}. \tag{15}$$

For unpolarized beam and target the reduced cross section from Eq. (13) can be expanded in terms of the hadronic structure functions:

$$\begin{aligned} \frac{d\sigma_{\gamma^* p}}{d\Omega^*_\pi} = \frac{|\mathbf{p}^*_\pi|}{K} \Bigg[&\frac{d\sigma_{\mathrm{T}}}{d\Omega^*_\pi} + \varepsilon \frac{d\sigma_{\mathrm{L}}}{d\Omega^*_\pi} + \varepsilon \frac{d\sigma_{\mathrm{TT}}}{d\Omega^*_\pi} \cos 2\phi^*_\pi \\ &+ \sqrt{2\varepsilon(\varepsilon+1)} \frac{d\sigma_{\mathrm{LT}}}{d\Omega^*_\pi} \cos\phi^*_\pi \Bigg]. \end{aligned} \tag{16}$$

Here, $\mathbf{p}^*_\pi$ is the pion momentum and $K = (W^2 - m_p^2)/2W$ is the photon equivalent energy in the c.m. frame of the subprocess $\gamma^* p \to p\pi^0$. Additionally, $\sigma_{\mathrm{T}} + \varepsilon\sigma_{\mathrm{L}}$, σ_{LT}, and σ_{TT} are, respectively, the structure functions that describe the transverse, longitudinal, longitudinal-transverse interference, and transverse-transverse interference components of the differential cross section.

Each of these structure functions contains the $\cos\theta^*_\pi$ dependence and can be parametrized in terms of the multipole amplitudes $E_{l\pm}$, $M_{l\pm}$, and $S_{l\pm}$ that describe the electric, magnetic, and scalar multipoles, respectively. The scalar multipoles $S_{l\pm}$ can be written in terms of the longitudinal multipoles $L_{l\pm} = \frac{\omega^*}{|\mathbf{q}^*|} S_{l\pm}$, where ω^* and $\mathbf{q}^*$ are the energy and 3-momentum of the virtual photon in the c.m. frame, respectively [2].

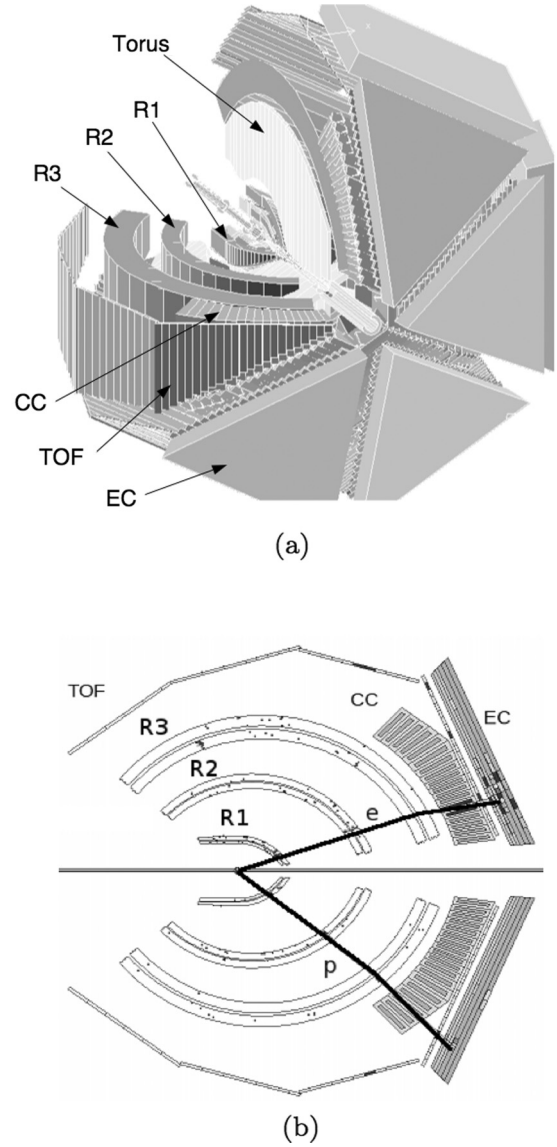

FIG. 2. (a) A three-dimensional view of CLAS showing the superconducting coils of the torus, the three regions of drift chambers (R1–R3), the Čerenkov counters, the time-of-flight system, and the electromagnetic calorimeters. The positive $\hat{Z}$ axis is out of the page along the symmetry axis. (b) A schematic view of a typical near-threshold event showing the reconstructed electron and proton tracks with the corresponding detector hits in two opposite CLAS sectors. The π^0 is reconstructed using the missing mass technique as discussed in the text.

III. EXPERIMENT

The near-threshold reaction $ep \to ep\pi^0$ was studied using the CEBAF Large Acceptance Spectrometer (CLAS) in Jefferson Lab's Hall-B [17]. Figure 2(a) shows the detector components that comprise CLAS. Six superconducting coils of the torus divide CLAS into six identical sectors and produce a toroidal magnetic field in the azimuthal direction around the beam axis. Each of the six sectors contain three regions of drift chambers (R1, R2, and R3) to track charged particles and to reconstruct their momentum [18], scintillator

counters for identifying particles based on time-of-flight (TOF) information [19], Čerenkov counters (CC) to identify electrons [20], and electromagnetic counters (EC) to identify electrons and neutral particles [21]. The CC and EC are used for triggering on electrons and provide a mechanism to separate charged pions and electrons. With these six sectors, CLAS provides a large solid angle coverage with typical momentum resolutions of about 0.5%–1.0% depending on the kinematics [17].

A 5.754-GeV electron beam with an average intensity of 7 nA was incident on a 5-cm-long liquid hydrogen target, which was placed 4 cm upstream of the CLAS center. Figure 2(a) shows the electron beam entering CLAS from the top left and exiting from the bottom right through the symmetry axis. A small nonsuperconducting magnet (minitorus) surrounded the target and generated a toroidal field to shield the R1 drift chambers from low energy electrons of high intensity. These electrons originated primarily from the Møller scattering process. The data used in this experiment were collected from October 2001 to January 2002 and the integrated luminosity was about 0.28 fb^{-1}. The electron beam energy of 5.754 GeV as determined in this experiment agrees within 6 MeV with an independent measurement in Hall A [22].

IV. ANALYSIS

At the start of this analysis, a cut of $W < 1.3$ GeV is applied to focus our events only in the kinematic region of interest. In this analysis the scattered electrons and protons are detected using CLAS and the π^0 is reconstructed using 4-momentum conservation. A typical event for this experiment is shown in Fig. 2(b).

A. Particle identification: Electron

The scattered electrons in the final state of the reaction are detected by requiring geometrical coincidence between the Čerenkov counters and the electromagnetic calorimeter in the same sector. The momentum of the electrons is reconstructed using the drift chambers. Using the energy deposited in the EC and the momentum, the electrons are isolated from most of the minimum ionizing particles (MIPs), e.g., pions, contaminating the electron spectra.

As electrons pass through the EC, they shower with a total energy deposition E_{tot} that is proportional to their momenta p. The sampling fraction energy E_{tot}/p is plotted as a function of momentum for each sector after applying all the other electron identification cuts. Figure 3 shows this distribution for one of the CLAS sectors for experimental and Monte Carlo simulated events. In the figure, one can note the MIPs contamination near the smaller values of E_{tot}/p. This contamination is significantly larger in data than in simulated events. The electrons are concentrated near $E_{\text{tot}}/p \approx 0.3$. Ideally, they should not show any dependence on momentum, albeit a slight momentum dependence is visible in the data. This dependence is parametrized and a cut of 3σ is applied as shown in the figure. The MIP events are well separated from the electrons below the 3σ cut.

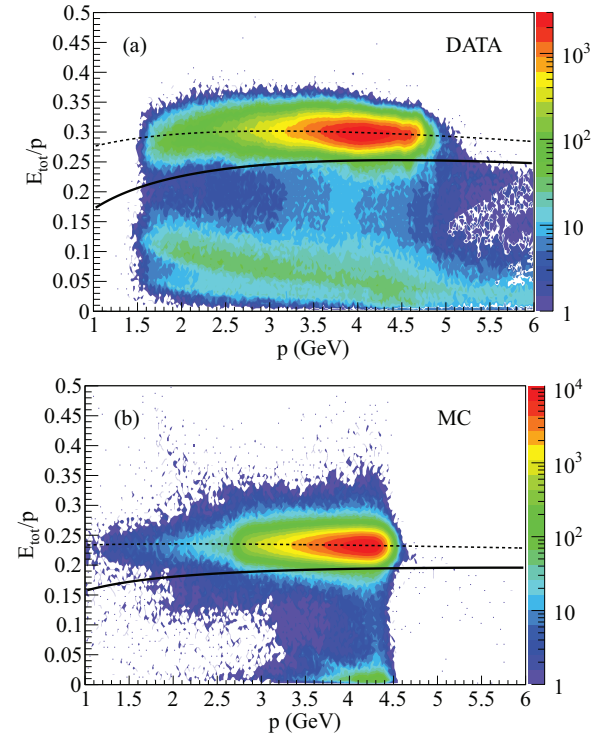

FIG. 3. (Color online) EC sampling fraction as a function of electron momentum for one of the CLAS sectors for (a) data and (b) Monte Carlo (MC) simulation. The dashed lines show the parametrized mean and the solid line indicates the 3σ cut.

B. Particle identification: Proton

The recoiled protons are identified using the measured momentum and the timing information obtained from the TOF counters. A track is selected as a proton whose measured time is closest to that expected of a real proton, i.e.,

$$\Delta t = t_{\text{meas}} - t_{\text{calc}} = (t_{\text{TOF}} - t_{\text{tr}}) - \frac{l}{\beta_{\text{calc}} c}. \qquad (17)$$

In the above equation, t_{TOF} is the time measured from the TOF counters, l is the distance from the target center to the TOF paddle, and t_{tr} is the event start time calculated from the electron hit time from the TOF traced back to the target position. Also, in Eq. (17) $\beta_{\text{calc}} = p/\sqrt{M_{\text{pdg}}^2 + p^2}$, where β_{calc} is computed using the PDG [23] value of the mass of the proton M_{pdg} and the momentum of the track p.

Figures 4(a) and 4(b) show the experimental and simulated event distributions, respectively, of Δt as a function of p for one of the CLAS sectors. The protons are centered around $\Delta t = 0$ ns and have a slight momentum dependence for $p <$ 1 GeV. The dashed lines indicate the parametrized mean of the distributions and the solid lines indicate the $\pm 3.5\sigma$ cut applied to select the protons.

C. Fiducial cuts and kinematic corrections

For perfect beam alignment, the incident electron beam is expected to be centered at $(X_{\text{beam}}, Y_{\text{beam}}) = (0, 0)$ cm at the target. However, owing to misalignments, the electron beam

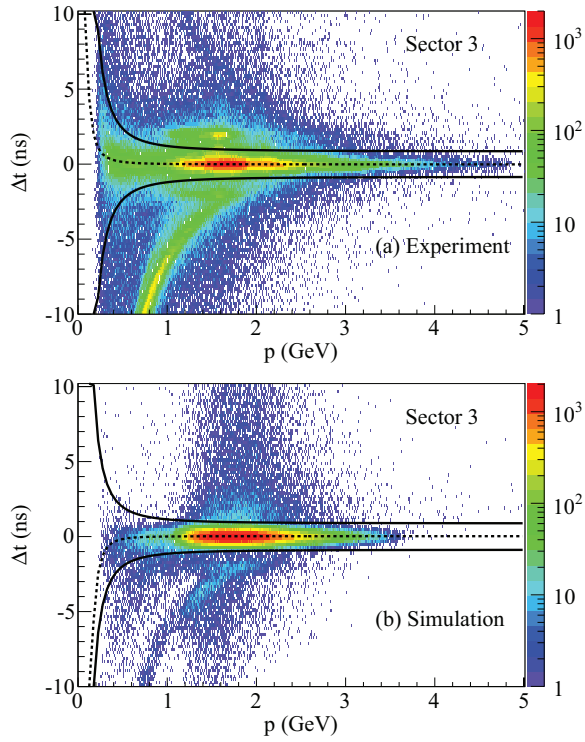

FIG. 4. (Color online) Δt as a function of p. The curves show the $\pm 3.5\sigma$ cut (solid lines) from the mean fit (dashed line) for one of the CLAS sectors for (a) experimental and (b) Monte Carlo simulated events.

was actually at $(X_{\text{beam}}, Y_{\text{beam}}) = (0.090, -0.345)$ cm. This misalignment of the beam axis is corrected for each sector, which also subsequently changes the reconstructed z-vertex positions of the electron and proton tracks. The details of this correction are described in previous works [24,25]. A cut of $z \in (-8.0, -0.8)$ cm is placed on the z-vertex to isolate events from within the target cell.

The measured angles and momenta of the electrons and protons are corrected using the same method as used in previous analyses [24,25].

The electrons start to lose energy as they enter the electromagnetic calorimeter. When the electrons shower near the edge of the calorimeter, their shower is not fully contained and so their energies cannot be properly reconstructed. As such, a fiducial cut is applied to remove these events.

Electrons give off Čerenkov light in the CC, which is collected in the PMTs on either side of the counters in each sector. Inefficient regions in the CC are isolated by removing those regions where the average number of photoelectrons $\langle N_{\text{phe}} \rangle < 5$. This cut results in keeping all events that lie in regions where the CC efficiency is about 99% [20].

To deal with edges and holes in the drift chambers, and to remove dead or inefficient wires, a fiducial cut for both electrons and protons is applied. Regions of nonuniform acceptance in the azimuthal angle ϕ resulting from these attributes are isolated on a sector-by-sector basis as a function of the electron's momentum p_e and polar angle θ_e. For the electron, at fixed p_e and θ_e, one expects the angular distribution to be symmetric in ϕ_e and relatively flat. Empirical cuts are

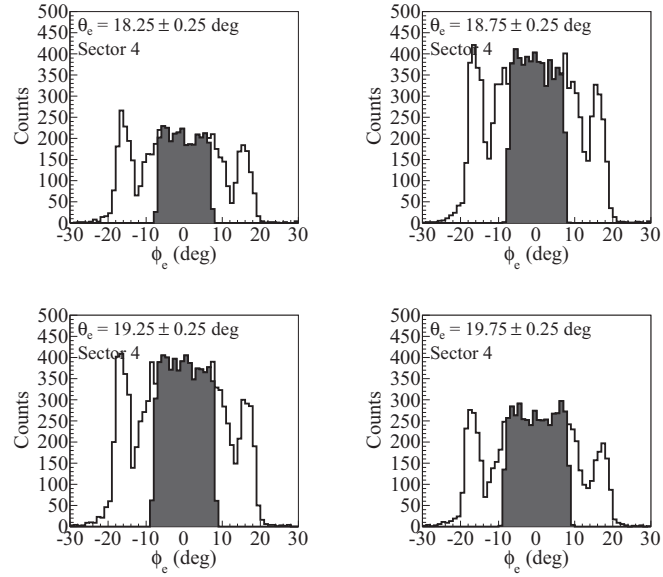

FIG. 5. Electron ϕ_e distribution for CLAS Sector 4 for $p_e = 4.1 \pm 0.1$ GeV shown for different θ_e slices. The unshaded curves show ϕ_e distribution after electron selection and the shaded curves show the ϕ_e distribution after applying electron drift chambers fiducial cuts.

applied to select these regions of relatively flat ϕ_e as shown in Fig. 5 for electrons with $p = 4.1 \pm 0.1$ GeV for different slices of θ_e and one of the CLAS sectors. The same cuts are applied to both experimental and simulated events.

As for electrons, a fiducial cut on the proton's azimuthal angle ϕ_p as a function of its momentum p_p and polar angle θ_p is applied. However, the edges of the ϕ_p distributions are asymmetric for different slices of θ_p. The upper and lower bounds on ϕ_p are extracted and parametrized as a function of θ_p and p_p. The result of this cut for one of the CLAS sectors is shown in Fig. 6.

D. Background subtraction and π^0 identification

The neutral pion in the final state is reconstructed using energy and momentum conservation constraint. To do so, we use the conservation of 4-momentum and look at the missing

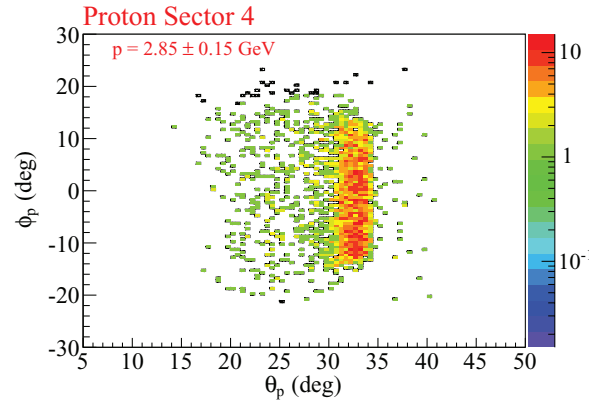

FIG. 6. (Color online) Proton ϕ_p vs θ_p distribution for CLAS Sector 4 for $p_p = 2.85 \pm 0.15$ GeV. Rejected tracks are shown in black.

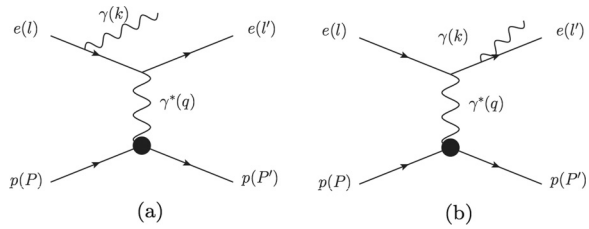

FIG. 7. The Bethe-Heitler process $ep \to ep\gamma$ diagrams for (a) a photon emitted from an incident electron (preradiation) and for (b) a photon emitted from a scattered electron (postradiation).

mass squared distribution of the detected particles (i.e., the electron and the proton):

$$M_X^2(ep) = (l + P - l' - P')^2. \tag{18}$$

Here, l, P, l', and P' are 4-momenta of the incident and scattered particles as described in Sec. II.

There are several difficulties in the analysis in the near-threshold region. In this region, the pion electroproduction cross section goes to zero; so, the statistics are very low. Also, a major source of contamination to the neutral pion signal near threshold is the elastic Bethe-Heitler process $ep \to ep\gamma$. The two dominating Feynman diagrams for this process are shown in Fig. 7. Figure 7(a) shows the diagram with a preradiated photon (emission from an incident electron) and Fig. 7(b) shows the diagram with a postradiated photon (emission from a scattered electron). These photons are emitted approximately in the direction of the incident and scattered electron, respectively [26,27]. When these photons are emitted, the incident and scattered electrons lose energy. This feature of the Bethe-Heitler process can be exploited to our benefit.

For the elastic process $ep \to ep$, the proton angle can be computed independently of the incident or scattered electron energies:

$$\tan\theta_1^p = \frac{1}{\left(1 + \frac{E'}{m_p - E'\cos\theta_e'}\right)\tan\frac{\theta_e'}{2}}, \tag{19}$$

$$\tan\theta_2^p = \frac{1}{\left(1 + \frac{E}{m_p}\right)\tan\frac{\theta_e'}{2}}. \tag{20}$$

Here, θ_1^p and θ_2^p are the proton angles computed independently of the incident or scattered electron energies, respectively. Also, θ_e' is the angle of the scattered electron in the laboratory frame, and E and E' are the energies of the incident and scattered electron, respectively. We can calculate these angles for each event and look at its deviation ($\Delta\theta_{1,2}^p$) from the measured value (θ_{meas}^p):

$$\Delta\theta_{1,2}^p \equiv \theta_{1,2}^p - \theta_{\text{meas}}^p. \tag{21}$$

Figure 8(a) shows the M_X^2 plotted as a function of this deviation $\Delta\theta_1^p$ for one of the near-threshold regions, $W = 1.09 \pm 0.01$ GeV. In the plot, we see two red spots along $M_X^2 = 0\,\text{GeV}^2$. The one on the left is centered along $\Delta\theta_1^p = 0^\circ$, corresponding to the preradiated photon events. The other corresponds to the postradiated photon events. Additionally, these radiative events are also present in the positive M_X^2.

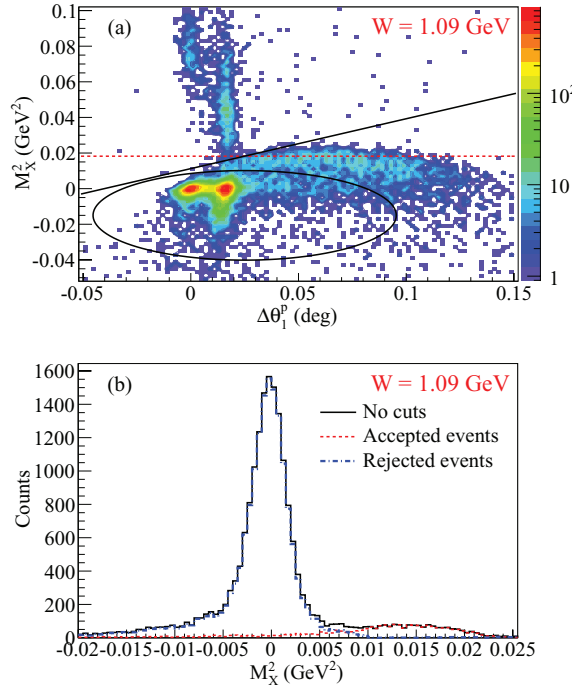

FIG. 8. (Color online) (a) M_X^2 vs $\Delta\theta_1^p$ for $W = 1.09 \pm 0.01$ GeV. The red dashed line indicates the expected pion peak position. The left red spot centered around zero degrees corresponds to the elastic scattering events in which the incident electrons have undergone Bethe-Heitler radiation (preradiative) and the one on the right to the elastic postradiative events. The events below the linear polynomial and outside the ellipse are selected as pions. (b) M_X^2 for events with $W = 1.09 \pm 0.01$ GeV. The black solid curve shows events prior to any Bethe-Heitler subtraction cuts, the blue dash-dotted curve shows events rejected from the cuts, and the red dashed curve shows those events that survive the Bethe-Heitler subtraction cuts.

These are the radiative events that we need to isolate from the pion signal as indicated by the red dashed line in the plot. An ellipse and a linear polynomial are used to reject these events. These cuts are parametrized as a function of W. The result of these cuts is seen in Fig. 8(b) with the accepted events after the cut shown in red (dashed curve) as our pions and the rejected events in blue (dash-dotted curve).

After the Bethe-Heitler subtraction cuts are applied, the pions are selected by making a $\pm 3\sigma$ cut on M_X^2 from the mean position of the distribution. An example of the distributions and fit are shown in Fig. 9. The M_X^2 distributions (black circles) are fit with two Gaussians. The blue (dash-dotted) curve is an estimate of the remaining Bethe-Heitler background in the M_X^2 distribution, which was not eliminated by the elliptical cuts of Fig. 8(a). This was subtracted to yield the green (triangle) points. A systematic uncertainty of $\pm 8\%$ is associated with this background subtraction procedure, which is detailed in Sec. VII.

V. SIMULATIONS

To determine the cross section, a Monte Carlo simulation study is required, including a physics event generator and the detector geometry. Events are generated using the

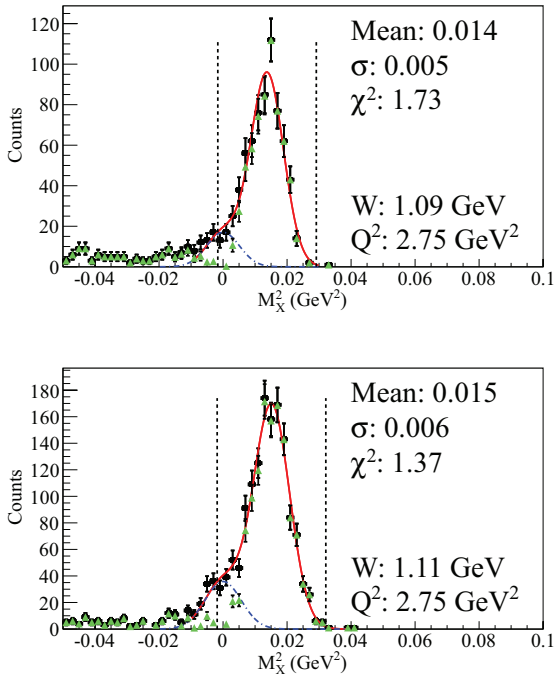

FIG. 9. (Color online) An example of the $M_X^2(ep)$ distribution with a double Gaussian fit after applying the elliptical cuts (black circles) of Fig. 8(a) and after residual Bethe-Heitler and other contamination subtractions (green triangles) for $Q^2 = 2.75 \pm 0.25\ \mathrm{GeV}^2$ and $W = 1.09 \pm 0.01$ GeV (top) and $W = 1.11 \pm 0.01$ GeV (bottom) integrated over all ϕ_π^* and $\cos\theta_\pi^*$. The black dashed lines indicate the $\pm 3\sigma$ cuts applied to select the pions. The χ^2 is the goodness of fit per degree of freedom. See Sec. IV D for details.

MAID2007 unitary isobar model (UIM) [28], which uses a phenomenological fit to previous photo- and electroproduction data. Nucleon resonances are described using Breit-Wigner forms and the nonresonant backgrounds are modeled from Born terms and t-channel vector-meson exchange. To describe the threshold behavior, Born terms were included with mixed pseudovector-pseudoscalar πNN coupling [28]. While the pion electroproduction world data in the resonance region goes up to $Q^2 \sim 7\ \mathrm{GeV}^2$ [29] for $W > 1.11$ GeV, there are no data near threshold for $Q^2 > 2\ \mathrm{GeV}^2$ and $W < 1.11$ GeV (the kinematics of this work). Thus, cross sections for the kinematics of this work are described by extrapolations of the fits to the existing data in the MAID2007 model.

Events are generated to cover the entire kinematic range described in Table I. About 73×10^6 events are generated for the 2400 kinematic bins and 6.7×10^6 events were reconstructed after all analysis cuts. The average resolutions of the kinematic quantities, W, Q^2, $\cos\theta_\pi^*$, and ϕ_π^* are 0.014 GeV, 0.008 GeV^2, 0.05, and 8°, respectively. These resolutions are obtained by comparing the generated kinematic quantities with those after reconstruction.

TABLE I. Kinematic bin selection.

Variable	Range	No. of bins	Width
W (GeV)	1.08 : 1.16	4	0.02
Q^2 (GeV^2)	2.0 : 4.5	4	Variable
$\cos\theta_\pi^*$	−1 : 1	5	0.4
ϕ_π^* (deg)	0 : 360	6	60

After the physics events are generated, their passage through the detector is simulated using the GEANT3-based Monte Carlo (GSIM) program. This program simulates the geometry of the CLAS detector during the experiment and the interaction of the particles with the detector material. GSIM models the effects of multiple scattering of particles in the CLAS detector and geometric misalignments. The information for all interactions with the detectors is recorded in raw banks, which is used for reconstruction of the tracks.

The events from GSIM are fed through a program called the GSIM Post Processor (GPP) to incorporate effects of tracking resolution and dead wires in the drift chambers and timing resolutions of the TOF.

These events are then processed using the same codes as those events from the experiment to reconstruct tracks and higher level information such as 4-momentum, timing, and so on. The simulated events are analyzed the same way as the experimental data and are used to obtain acceptance corrections and radiative corrections for the cross-sections calculations.

VI. CORRECTIONS

A. Acceptance corrections

Acceptance corrections are applied to the experimental data to obtain the cross section for each kinematic bin. These corrections describe the geometrical coverage of the CLAS detector, inefficiencies in hardware and software, and resolution effects from track reconstruction.

By comparing the number of events in each kinematic bin from the physics generator and the reconstruction process, the acceptance can be obtained as

$$A_i = \frac{N_{\mathrm{rec}}^i}{N_{\mathrm{gen}}^i}, \tag{22}$$

where N_{rec}^i corresponds to those events that have gone through the entire analysis process including track reconstruction and all analysis cuts. N_{gen}^i are those events that were generated. Figure 10 shows the acceptances for a few of the near-threshold bins as a function of ϕ_π^*.

B. Radiative corrections

The radiative correction is obtained using the software package EXCLURAD [30] that takes theoretical models as input to compute the corrections. For this experiment the MAID2007 model, the same model used to generate Monte Carlo events, is used to determine the radiative corrections. The radiative corrections are closely related to the acceptance corrections. For each kinematic bin the differential cross section can be written as

$$\sigma = \frac{N_{\mathrm{meas}}}{\mathcal{L}\,A}\frac{1}{\delta}, \tag{23}$$

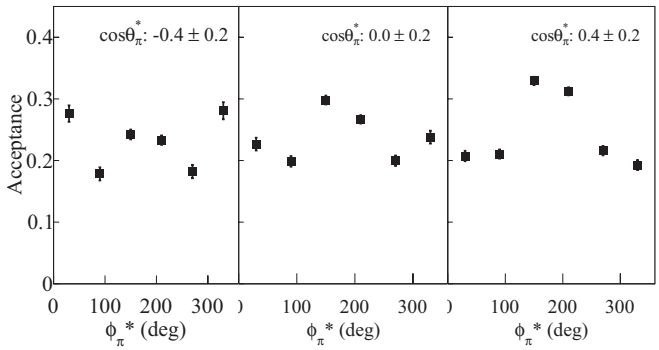

FIG. 10. Acceptance corrections for $W = 1.09$ GeV and $Q^2 = 2.75$ GeV^2 as a function of ϕ_π^*. Each subplot shows the correction for a different $\cos\theta_\pi^*$ bin.

where $N_{\rm meas}/\mathcal{L}$ is the number of events from the experiment normalized by the integrated luminosity (with appropriate factors) before acceptance and radiative corrections. Also, $A = N_{\rm rec}^{\rm RAD}/N_{\rm gen}^{\rm RAD}$ is the acceptance correction for the bin and δ is the radiative correction. It should be noted that the events for the acceptance correction were generated with a radiated photon in the final state using the MAID2007 model.

EXCLURAD uses the same model to obtain the correction $\delta = N_{\rm gen}^{\rm RAD'}/N_{\rm gen}^{\rm NORAD'}$, where $N_{\rm gen}^{\rm NORAD'}$ are events generated without a radiated photon in the final state. Thus,

$$\sigma = \frac{N_{\rm meas}}{\mathcal{L}} \left(\frac{N_{\rm gen}^{\rm RAD}}{N_{\rm rec}^{\rm RAD}}\right) \times \left(\frac{N_{\rm gen}^{\rm NORAD'}}{N_{\rm gen}^{\rm RAD'}}\right). \tag{24}$$

The details of the radiative correction procedure are described in Ref. [25].

Figure 11 shows the radiative corrections calculated for one of the kinematic bins as a function of the pion angles in the c.m. system. One can observe that the corrections have a ϕ_π^* dependence. This is because the bremsstrahlung process occurs only near the leptonic plane, i.e., at angles near 0° or 180° with respect to the hadronic plane. Also, one can notice that the correction increases with $\cos\theta_\pi^* \to -1$. This is because the cross section is expected to approach zero at

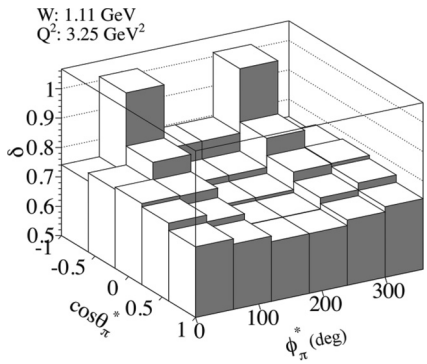

FIG. 11. The radiative corrections for $W = 1.11$ GeV and $Q^2 = 3.25$ GeV^2 as a function of $\cos\theta_\pi^*$ and ϕ_π^* obtained from EXCLURAD using the MAID2007 model.

backwards angles and that is the region where the Bethe-Heitler events dominate. The average radiative correction over all kinematic bins is ∼25%.

C. Other corrections

Two other corrections were applied to the cross section. One of them involves estimating the fraction of the events originating from the target cell walls and the other is an empirical overall normalization factor.

To estimate the level of contamination from the target cell walls, events collected during the empty-target run period of the experiment are analyzed using the same process as those for the production run period. Only those events that fall within the target wall region for the empty target should be considered for the source of contamination. This is because even though there was no liquid hydrogen in the target, it was still filled with cold hydrogen gas. So, for this estimation only events within ±0.5 cm of the target wall region are selected. The correction is then calculated by taking the ratio of events within this target region from the empty target runs to those from the production run normalized to the total charge, ρ, collected during the run periods,

$$R = \frac{N_{\rm empty\ target}}{N_{\rm production}} \frac{\rho_{\rm production}}{\rho_{\rm empty\ target}}. \tag{25}$$

The average contamination is approximately 1%–1.9%, depending on the W kinematic bin. This ratio is then applied as a correction factor to the measured cross section $\sigma = \sigma_{\rm meas}(1 - R)$. Here, σ is the corrected cross section and $\sigma_{\rm meas}$ is the measured cross section for a particular bin in W.

The second correction (the empirical overall normalization factor) comes from comparing the measured $ep \to ep$ elastic and the $ep \to ep\pi^0$ cross sections in the $\Delta(1232)$ resonance region ($W = 1.23$ GeV) to previously measured values [24,28,31,32]. The measured elastic scattering cross section from this experimental data was compared to the known cross-section values [31], where both the electron and the proton were detected in the final state. A deviation of ∼11% from the known cross section values is observed.

This deviation of ∼11% from the known elastic electron-proton scattering cross section includes the inefficiencies associated with the proton detection in CLAS [17,33].

To account for this discrepancy, an overall normalization factor of $R_{\rm elastic} = 0.89$ is applied to the $ep \to ep\pi^0$ differential cross section for every kinematic bin. An associated systematic uncertainty of ±5% is applied. After this correction is applied, the measured $ep \to ep\pi^0$ cross sections for the $\Delta(1232)$ resonance region, $W = 1.23 \pm 0.01$ GeV, are in agreement with previous measurements [24,28,32] to within 5% on average. Figure 12 shows the result of this correction for a few kinematic bins in the $\Delta(1232)$ resonance region.

Because the threshold region of interest for this experiment is sandwiched between the elastic and the $\Delta(1232)$ resonance region and the results in these two regions are consistent with previous measurements after applying this overall normalization factor, we believe this procedure is justified. This correction to the cross section also includes any detector inefficiencies and, as such, these inefficiencies will not be accounted for separately.

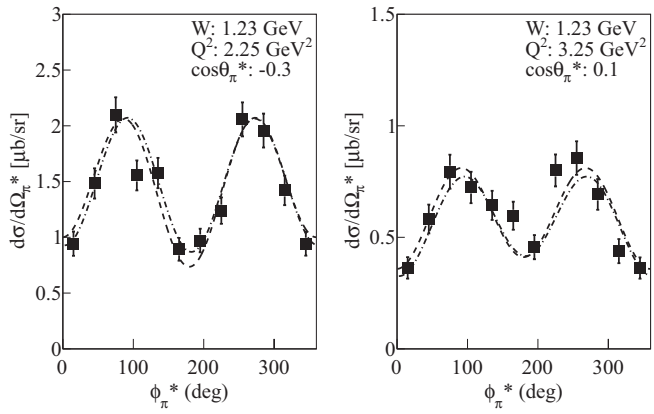

FIG. 12. The differential cross section $ep \to ep\pi^0$ for the $\Delta(1232)$ resonance region, $W = 1.23 \pm 0.01$ GeV, for typical kinematic bins. The squares are the measured cross sections after applying the normalization correction factor (see text for details). The dashed curves are from Ref. [32] and the dash-dotted curves are from the MAID2007 model. The corrected values agree with the two curves to within 5% on average.

VII. SYSTEMATIC STUDIES

To determine the systematic uncertainties in the analysis, the parameters of the likely sources of those uncertainties are varied within reasonable bounds and the sensitivity of the final result is checked against this variation. A summary of the systematic uncertainties averaged over the kinematic bins of interest is shown in Table II.

The electron and proton identification cuts, the electron fiducial cuts, the vertex cuts and the target cell correction cuts provide small contributions to the overall systematic uncertainties.

The electron EC sampling fraction cuts were varied from 3σ to 3.5σ and the extracted structure functions changed by about 0.4% on average. The parameters for the electron fiducial cuts were similarly varied by about 10% and the structure functions changed by about 1% on average. As such, a systematic uncertainty of 0.4% and 1% was assigned to these sources.

TABLE II. The average systematic uncertainties for the differential cross sections from various sources and the corresponding criteria. The final quoted systematic uncertainty, obtained by adding the different systematic uncertainties from each source in quadrature, is about 10.8%.

Source	Estimate (%)
e^- EC sampling fraction cuts	0.4
e^- fiducial cuts	1
p Δt cuts	1.1
Vertex cuts	0.1
Background subtraction cuts	8
π^0 M_X^2 cut	3
Target cell correction	1
Elastic normalization correction	5
Acceptance and radiative correction	4
Total	10.8

The Δt cuts to select the protons were varied from 3.5σ to 4σ and a variation of about 1.1% on average was observed on the extracted structure functions, which was assigned as the systematic uncertainty associated with this source. The variations in the fiducial cuts for the proton had a negligible effect on the structure functions.

The vertex cuts were reduced by 5% and a variation of about 0.1% on average was observed on the extracted structure functions. So, a systematic uncertainty of 0.1% was assigned to this source. The structure functions are compared before and after applying the target cell corrections. A variation of about 1% is observed and this value was assigned as a source of systematic uncertainty.

The major sources of systematic uncertainty are the Bethe-Heitler background subtraction, the missing mass squared cut to select the neutral pions, the elastic normalization corrections and the model dependence of the acceptance and radiative corrections.

There are residual Bethe-Heitler events that escape the elliptical Bethe-Heitler cuts. These events peak at $M_X^2 = 0$, which have to be included in the overall fit. A Gaussian distribution was assumed for both the π^0 and the remaining Bethe-Heitler events. The pions are modeled by a Gaussian distribution near the expected pion mass and the Bethe-Heitler events are modeled by a Gaussian whose peak is at $M_X^2 = 0$. This accounts for much of the tail in Figs. 8(b) and 9. The resolution for M_X^2 for the Bethe-Heitler and the pion distributions is expected to be similar because of the same kinematics of the detected electron and the proton. The Gaussian fit for the Bethe-Heitler is obtained, which is then subtracted to yield the pions.

To see the effect of the background subtraction, the structure functions were compared with and without the application of the Bethe-Heitler background subtraction cuts. The structure functions changed by about 8% on average and this was used as a systematic uncertainty for this procedure.

The missing mass squared cut was varied from 3σ to 4σ and this resulted in a change of about 3% on average in the extracted structure functions.

The systematic uncertainty on the elastic normalization correction of $\pm 5\%$ was obtained by looking at the difference between the extracted structure functions before and after applying the correction factor to the data. The structure functions varied by about 5% on average.

Additionally, a $\pm 4\%$ systematic uncertainty is assigned on the model dependence of the acceptance and radiative corrections based on previous analyses [15,24,25].

The total average systematic uncertainty, obtained by adding the individual contributions in quadrature is 10.8%.

VIII. DIFFERENTIAL CROSS SECTIONS AND STRUCTURE FUNCTIONS

The kinematic coverage of the experiment spans over W from 1.08 to 1.16 GeV and Q^2 from 2 to 4.5 GeV^2. The reduced differential cross section for the reaction is computed for each kinematic bin. The cross sections are reported at the center of each kinematic bin. Figure 13 shows the differential cross section for some of the kinematic bins near threshold as a

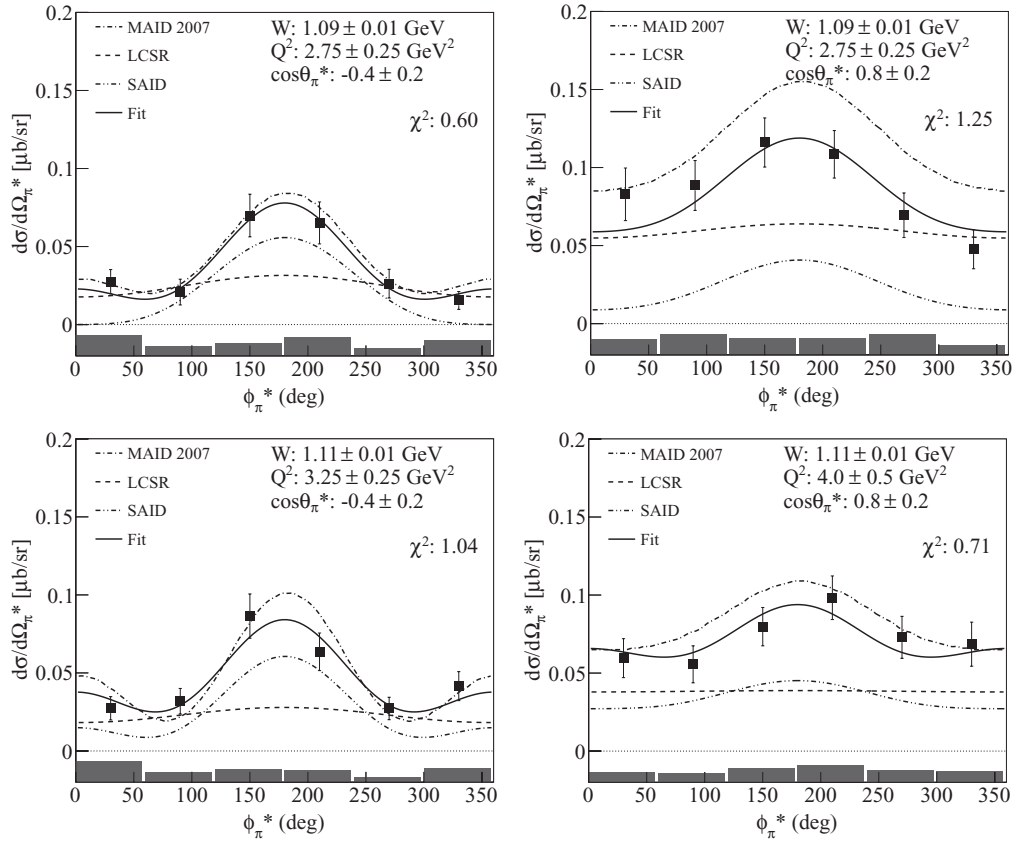

FIG. 13. The differential cross sections in μb/sr for a few kinematic bins near threshold as a function of ϕ_π^*. Experimental points (squares) are shown with statistical uncertainties only. The sizes of the estimated systematic uncertainties are shown in gray boxes below. The predictions from LCSR, MAID2007, and SAID are shown as dashed, dash-dotted, and dash-double-dotted curves, respectively. The horizontal line at zero serves as a visual aid. The fit to the distributions is shown as a solid curve. See Sec. VIII for details.

function of ϕ_π^*. The predictions from LCSR [14], MAID2007 [28], and SAID [34] are shown for comparison.

Using Eq. (16), the differential cross section is fitted to extract the structure functions $\sigma_T + \varepsilon\sigma_L$, σ_{TT}, and σ_{LT}. The result of the fit is shown as the solid curve in Fig. 13. The reduced χ^2 for the fit is calculated using $\chi^2 = \chi_0^2/\nu$, where ν is the number of degrees of freedom calculated for each W, Q^2, and $\cos\theta_\pi^*$ bin (i.e., $\nu = 6$ data points -3 fit parameters $= 3$), and χ_0^2 is the un-normalized goodness of fit. The averaged χ^2 of the fits is 0.9.

The extracted structure functions $\sigma_T + \varepsilon\sigma_L$, σ_{TT}, and σ_{LT} are shown in Figs. 14–16, respectively, as a function of $\cos\theta_\pi^*$ for $W = 1.08$–1.16 GeV and $Q^2 = 2.0$–4.5 GeV^2. The data points are shown with statistical error bars only and the size of the systematic errors is shown as the gray boxes. Predictions from LCSR, MAID2007, and SAID are also included for $\sigma_T + \varepsilon\sigma_L$ and σ_{LT}. Because the LCSR does not include any σ_{TT} contributions in the calculations, they are not shown.

The structure function $\sigma_T + \varepsilon\sigma_L$ (Fig. 14) is generally in good agreement with the MAID2007 predictions but there is some discrepancy for $W = 1.09$ GeV at high $\cos\theta_\pi^*$. This discrepancy is reduced for higher W bins. The results disagree with the LCSR predictions, especially for those bins away from threshold ($W > 1.09$ GeV). This disagreement is also apparent for low Q^2 bins. As one moves closer to threshold and at high Q^2, the agreement is quite good, especially at backward angles $\cos\theta_\pi^* \to -1$. The LCSRs have been calculated and tuned especially for the threshold region at high Q^2 and, thus, there exists a strong disagreement at higher W and low Q^2 bins. The predictions from SAID strongly disagree for the first W bin and low Q^2 bins, but converge toward the MAID2007 predictions for higher W and Q^2.

The structure function σ_{TT} (Fig. 15) results are in good agreement with the SAID and MAID2007 predictions for low W and high Q^2 but disagree at high W and low Q^2 bins. Most of the values are close to zero for all W. The LCSR predictions assume only s-wave contributions to the cross section from this structure function. The d-wave contribution to the total cross sections in SAID range from 0 to 0.001μb for the near-threshold bins [34].

The structure function σ_{LT} (Fig. 16) also shows good agreement with the MAID2007 and LCSR predictions for high Q^2 and low W, but there is some discrepancy at other kinematics. The SAID prediction has a large disagreement at low W and Q^2, but the level of agreement at other kinematics is similar to the MAID2007 model.

IX. S-WAVE MULTIPOLES AND GENERALIZED FORM FACTORS

To compare with the calculated generalized form factors of Ref. [14], one must extract the s-wave multipole

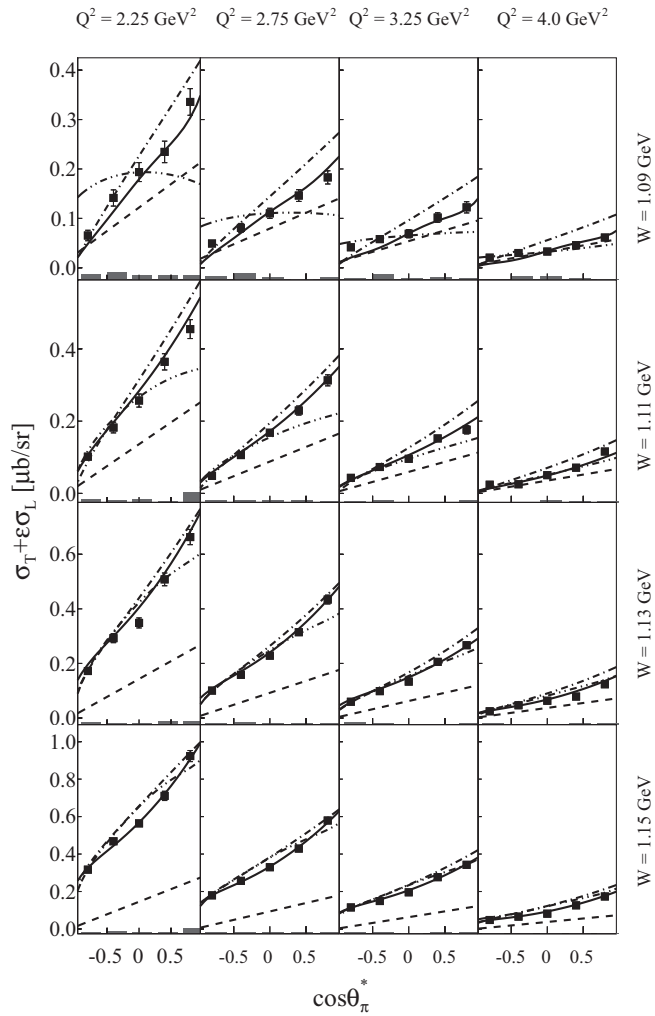

FIG. 14. The structure function $\sigma_T + \varepsilon\sigma_L$ as a function of $\cos\theta^*_\pi$ in μb/sr for $W = 1.08$–1.16 GeV and $Q^2 = 2.0$–4.5 GeV^2. Predictions from LCSR that include only s-wave contribution (dashed line), MAID2007 (dash-dotted line), and SAID (dash-double-dotted line) are shown. The error bars represent statistical uncertainties only and the estimated systematic uncertainties are shown as gray boxes. The solid curve corresponds to the results obtained from the fit to the cross sections (see Sec. IX for details). The values of Q^2 (on top of the panels) and W (on the right side of the panels) are the central values of the bins.

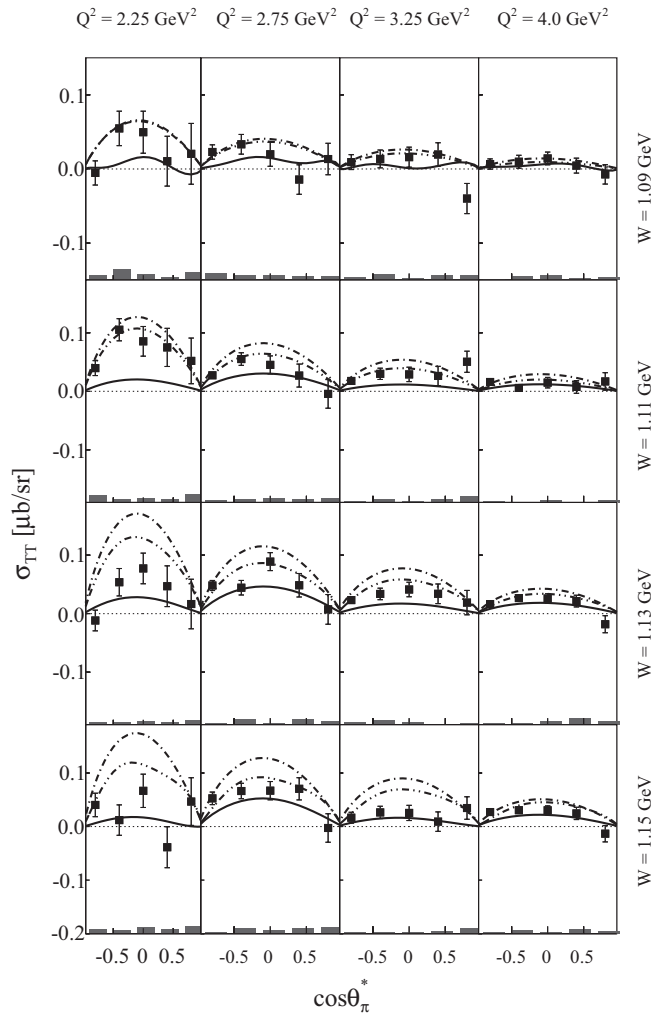

FIG. 15. The structure function σ_{TT} as a function of $\cos\theta^*_\pi$ in μb/sr for $W = 1.08 - 1.16$ GeV and $Q^2 = 2.0 - 4.5$ GeV^2. Predictions from MAID2007 (dash-dotted line) and SAID (dash-double-dotted line) are shown. The LCSR predictions do not include any σ_{TT} contributions, so they are not shown. The error bars represent statistical uncertainties only and the estimated systematic uncertainties are shown as gray boxes. The solid curve corresponds to the results obtained from the fit to the cross sections (see Sec. IX for details). The values of Q^2 (on top of the panels) and W (on the right side of the panels) are the central values of the bins. The horizontal line at zero serves as a visual aid.

amplitudes from the measured cross sections. First, the structure functions are written in terms of the helicity amplitudes H_i. The helicity amplitudes are functions defined by transitions between eigenstates of the helicities of the nucleon and the virtual photon [16]. The helicity amplitudes are then expanded in terms of the multipole amplitudes.

The structure functions are related to the helicity amplitudes $H_{1,2,\ldots,6}(W, Q^2, \cos\theta^*_\pi)$ by

$$\sigma_T = \tfrac{1}{2}(|H_1|^2 + |H_2|^2 + |H_3|^2 + |H_4|^2), \quad (26)$$

$$\sigma_L = |H_5|^2 + |H_6|^2, \quad (27)$$

$$\sigma_{TT} = \mathrm{Re}(H_3 H_2^* - H_4 H_1^*), \quad (28)$$

$$\sigma_{LT} = -\frac{1}{\sqrt{2}}\mathrm{Re}[(H_1 - H_4)H_5^* + (H_2 + H_3)H_6^*]. \quad (29)$$

The analysis of the data is based on the following expansion of the helicity amplitudes over multipole amplitudes (see, for example, [35]):

$$H_1 = \frac{1}{\sqrt{2}}\sin\theta^*_\pi \cos\frac{\theta^*_\pi}{2}\sum(B_{l+} - B_{(l+1)-}) \times [P''_l(\cos\theta^*_\pi) - P''_{l+1}(\cos\theta^*_\pi)], \quad (30)$$

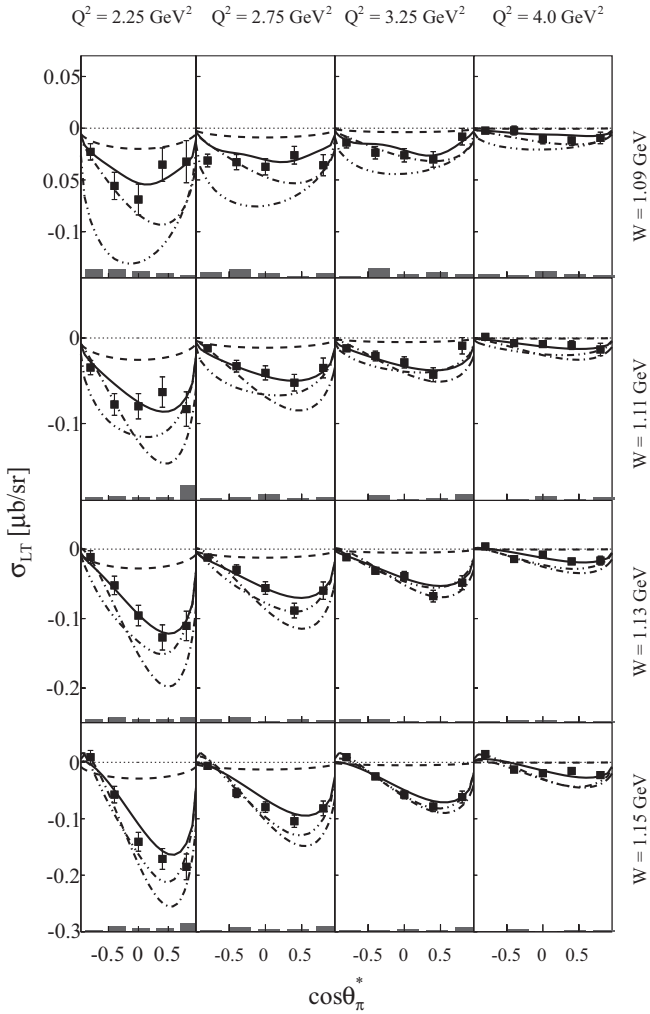

FIG. 16. The structure function $\sigma_{\rm LT}$ as a function of $\cos\theta_\pi^*$ in μb/sr for $W = 1.08$–1.16 GeV and $Q^2 = 2.0$–4.5 GeV^2. Predictions from LCSR that include only s-wave contribution (dashed line), MAID2007 (dash-dotted line), and SAID (dash-double-dotted line) are shown. The error bars represent statistical uncertainties only and the estimated systematic uncertainties are shown as gray boxes. The solid curve corresponds to the results obtained from the fit to the cross sections (see Sec. IX for details). The values of Q^2 (on top of the panels) and W (on the right side of the panels) are the central values of the bins. The horizontal line at zero serves as a visual aid.

$$H_2 = \sqrt{2}\cos\frac{\theta_\pi^*}{2}\sum(A_{l+} - A_{(l+1)-}) \times [P_l'(\cos\theta_\pi^*) - P_{l+1}'(\cos\theta_\pi^*)], \quad (31)$$

$$H_3 = \frac{1}{\sqrt{2}}\sin\theta_\pi^*\sin\frac{\theta_\pi^*}{2}\sum(B_{l+} + B_{(l+1)-}) \times [P_l''(\cos\theta_\pi^*) + P_{l+1}''(\cos\theta_\pi^*)], \quad (32)$$

$$H_4 = \sqrt{2}\sin\frac{\theta_\pi^*}{2}\sum(A_{l+} + A_{(l+1)-}) \times [P_l'(\cos\theta_\pi^*) + P_{l+1}'(\cos\theta_\pi^*)], \quad (33)$$

$$H_5 = \frac{Q}{|\mathbf{q}^*|}\cos\frac{\theta_\pi^*}{2}\sum(l+1)(S_{l+} + S_{(l+1)-}) \times [P_l'(\cos\theta_\pi^*) - P_{l+1}'(\cos\theta_\pi^*)], \quad (34)$$

$$H_6 = \frac{Q}{|\mathbf{q}^*|}\sin\frac{\theta_\pi^*}{2}\sum(l+1)(S_{l+} - S_{(l+1)-}) \times [P_l'(\cos\theta_\pi^*) + P_{l+1}'(\cos\theta_\pi^*)]. \quad (35)$$

Here, $P'_{l,l+1}(\cos\theta_\pi^*)$ and $P''_{l,l+1}(\cos\theta_\pi^*)$ are the first and second derivatives of the Legendre polynomials, respectively, and $\mathbf{q}^*$ is the virtual photon 3-momentum in the c.m. system. Also,

$$A_{l+} = \tfrac{1}{2}\left[(l+2)E_{l+} + lM_{l+}\right], \quad (36)$$

$$B_{l+} = E_{l+} - M_{l+}, \quad (37)$$

$$A_{(l+1)-} = \tfrac{1}{2}[(l+2)M_{(l+1)-} - lE_{(l+1)-}], \quad (38)$$

$$B_{(l+1)-} = E_{(l+1)-} + M_{(l+1)-}. \quad (39)$$

The strong $\cos\theta_\pi^*$ dependence of the structure function $\sigma_{\rm T} + \varepsilon\sigma_{\rm L}$ and the nonzero values of $\sigma_{\rm LT}$ found in the experiment (see Figs. 14 and 16) show that higher multipole amplitudes should be taken into account in addition to the s-wave amplitudes E_{0+} and S_{0+} at all W. Our understanding of the high-wave multipoles, which should be included in this analysis, was based on the results of the analysis of CLAS data [24,25] performed in Ref. [32] using the UIM and dispersion relations (DRs). These data are on the $\gamma^* p \to \pi^+ n$ [25] and $\gamma^* p \to \pi^0 p$ [24] cross sections in a similar range of Q^2 but in a significantly wider energy range, which start from $W =$ 1.15 and 1.11 GeV, respectively. The precision in the present experimental results near threshold is much better than the precision in Refs. [24,25]. However, the results of their analysis are useful to study the p- and d-wave contributions, which are determined mainly by the $\Delta(1232)P_{33}$, $N(1440)P_{11}$, and $N(1520)D_{13}$ resonances.

According to the results of the analysis [32] at $W = 1.09$ to 1.15 GeV, there are large p-wave contributions related to the $\Delta(1232)P_{33}$ and $N(1440)P_{11}$. The d-wave contributions are negligibly small for the following reasons: (i) near threshold, the d-wave multipole amplitudes are suppressed compared to the p-wave amplitudes by the additional kinematical factor p_π^*; (ii) at the values of Q^2 investigated in this experiment, the contribution of the $N(1520)D_{13}$ to the corresponding multipole amplitudes is significantly smaller than the contributions of the $\Delta(1232)P_{33}$ and $N(1440)P_{11}$ to the p-wave multipole amplitudes; (iii) in contrast with the $\Delta(1232)P_{33}$ and $N(1440)P_{11}$, the width of the $N(1520)D_{13}$ is significantly smaller than the difference between the mass of the resonance and total energy at the threshold. Therefore, in our analysis only multipole amplitudes E_{0+}, S_{0+}, $M_{1\pm}$, $S_{1\pm}$, and E_{1+} were included.

The data were fitted simultaneously at $W = 1.09, 1.11, 1.13,$ and 1.15 GeV with statistical and systematic uncertainties added in quadrature for each point. The amplitudes were parametrized according to their threshold behavior and the results of the analysis in Ref. [32].

Owing to the Watson theorem [36], the imaginary parts of the multipole amplitudes below the 2π production threshold are related to their real parts as $\mathrm{Im}\mathcal{M} = \mathrm{Re}\mathcal{M}\tan(\delta^I_{\pi N})$, where $\mathcal{M}$ denotes $E^I_{l\pm}$, $M^I_{l\pm}$, or $S^I_{l\pm}$ amplitudes, and I is the total isotopic spin of the πN system. Near threshold $\delta^I_{\pi N} \sim p_\pi^{*2l+1}$, and the imaginary parts of the multipole amplitudes are suppressed compared to their real parts. Therefore, in the analysis, only the real parts of the amplitudes were kept. These

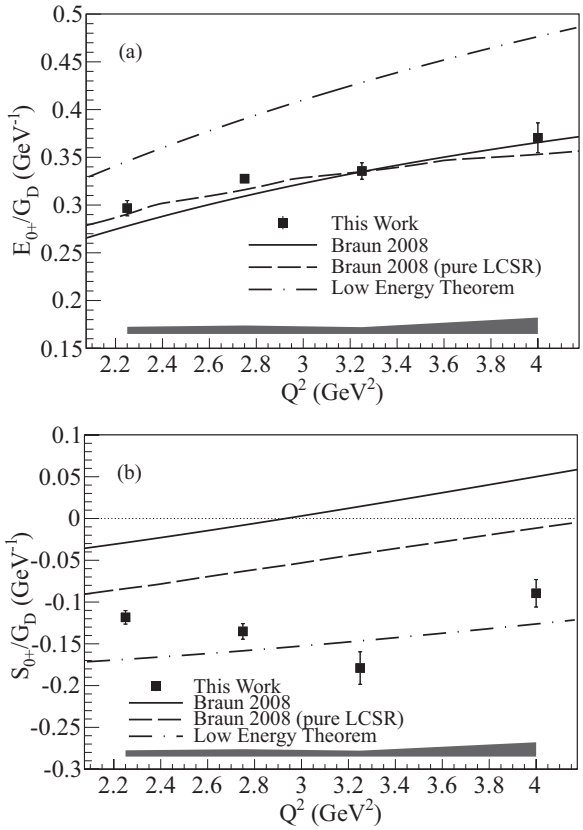

FIG. 17. The s-wave multipoles (a) E_{0+} and (b) S_{0+} normalized to the dipole formula G_D are plotted as a function of Q^2. The error bars include statistical and systematic uncertainties added in quadrature. The size of the estimated systematic uncertainties are shown at the bottom. The LCSR-based model predictions and the LET predictions are also shown as curves. The horizontal line at zero serves as a visual aid.

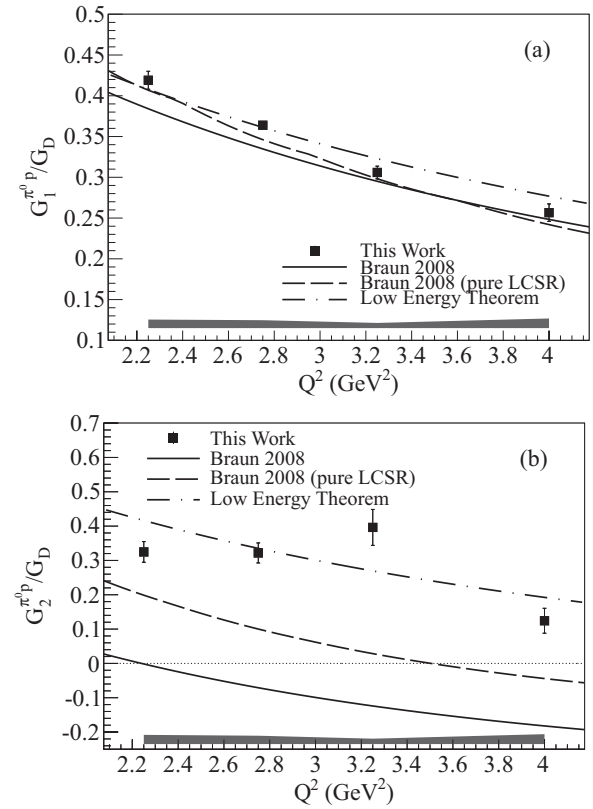

FIG. 18. The generalized form factors (a) $G_1^{\pi^0 p}$ and (b) $G_2^{\pi^0 p}$ normalized to the dipole formula G_D are plotted as a function of Q^2. The error bars include statistical and systematic uncertainties added in quadrature. The size of the estimated systematic uncertainties are shown in the bottom. The LCSR-based model predictions and the LET predictions are also shown as curves. The horizontal line at zero serves as a visual aid.

amplitudes were parametrized as follows: E_{0+}, $S_{0+} \sim$ const, $M_{1\pm}$, $S_{1\pm}$, and $E_{1+} \sim p_\pi^*$.

In the fitting procedure, the amplitudes E_{0+}, S_{0+}, and $M_{1\pm}$ were fitted without any restrictions. The relatively small amplitudes $S_{1\pm}$ and E_{1+} were fitted within ranges found from the results of the analysis of the data [24,25] using the UIM and DR in Ref. [32]. It should be mentioned that the results for the $M_{1\pm}$ contributions obtained in our fit of the $\gamma^* p \to \pi^0 p$ cross sections near threshold are consistent with those of Ref. [32] obtained in the analysis of significantly larger range over W. The overall average χ^2 per degree of freedom for the fit is approximately one.

The obtained results for the structure functions are plotted in Figs. 14–16 as solid curves. It can be seen that the multipole amplitudes E_{0+}, S_{0+}, $M_{1\pm}$, $S_{1\pm}$, and E_{1+} parametrized in the way discussed above represent the data very well at all W. The obtained results for E_{0+} and S_{0+} are presented in Fig. 17. These multipoles have been normalized to the dipole formula $G_D(Q^2) = (1 + \frac{Q^2}{0.71})^{-2}$.

Figure 18 shows the extracted generalized form factors, G_1 and G_2, as a function of Q^2. The error bars on the points include statistical and systematic uncertainties added in quadrature. The size of the estimated systematic uncertainties is shown separately at the bottom of the plots, which assumes all systematic errors for all the data points to be entirely uncorrelated (10.8%). The LET [7] predictions are shown as dash-dotted curves.

The plots also show LCSR predictions [14] as solid and dashed curves. Braun *et al.* have tried to minimize the uncertainties in their LCSR-based model calculations by including electromagnetic form factor values known from experiment. These calculations are shown as solid curves in the figure. The "pure" LCSR-based models are calculations where all the form factors are obtained entirely from theoretical calculations and the uncertainties have not been minimized. These are shown as dashed curves in the figure. The difference between these two curves can essentially be treated as the overall uncertainty in their predictions.

X. DISCUSSION

The results for the E_{0+} multipole and $G_1^{\pi^0 p}$ are in good agreement with the LCSR predictions. The extracted E_{0+} values deviate significantly from the LET predictions over the entire Q^2 range even though the extracted $G_1^{\pi^0 p}$ values are not too far off from the LET predictions. This is because

the LET calculations for E_{0+} only depend on $G_1^{\pi^0 p}$ [Eq. (5)], whereas the LCSR calculations include contributions from both $G_1^{\pi^0 p}$ and $G_2^{\pi^0 p}$ [Eq. (2)]. The overall trends of increasing E_{0+} and decreasing $G_1^{\pi^0 p}$ are similar to these two predictions, but the deviation of the extracted values for $G_1^{\pi^0 p}$ from the LET predictions becomes much more apparent at $Q^2 > 3$ GeV^2.

One can observe a discrepancy of our results for the S_{0+} multipole and $G_2^{\pi^0 p}$ from the LCSR predictions. The results are closer to the LET predictions but are not entirely consistent for all Q^2.

The uncertainty in the LCSR predictions for the S_{0+} multipole and $G_2^{\pi^0 p}$ is much bigger than for E_{0+} and $G_1^{\pi^0 p}$. In the chiral limit approximation, $m_\pi \to 0$, the Pauli form factor $F_2(Q^2)$, which is the primary contributor to the calculations of S_{0+} and $G_2^{\pi^0 p}$, is not reproduced very well. Also, the LCSR calculations exist in leading order only and do not include next-to-leading order (NLO) corrections. The NLO corrections are expected to be large. Additionally, the LCSR predictions contain approximations and were not expected to have an accuracy of better than 20% [14].

Furthermore, the LCSR predictions do not include effects from terms proportional to the pion mass. In the Q^2 region of this experiment, the predictions indicate a suppression of the S_{0+} multipole [14] and this multipole is very sensitive to corrections of all kinds, including the pion mass corrections. In the LET predictions, some pion mass corrections have been included [7]. This may also explain the discrepancy between the predictions and the extracted results for S_{0+} and $G_2^{\pi^0 p}$.

Owing to these theoretical uncertainties, the predictions of the magnitude of S_{0+} and $G_2^{\pi^0 p}/G_D$, and where they cross zero, differ for the two methods of calculation. The experimental results indicate that this sign change for $G_2^{\pi^0 p}/G_D$ occurs at $Q^2 > 4$ GeV^2 rather than at the LCSR prediction of around 2.2 or 3.5 GeV^2.

The results of the structure functions, Figs. 14–16, indicate a significant contribution of the p-wave in the near-threshold region as indicated by the almost linear dependence of the $\sigma_T + \varepsilon\sigma_L$ as a function of $\cos\theta_\pi^*$. This contribution increases as one moves away from threshold to higher W (e.g., see Fig. 16). This is highly underestimated in the overall LCSR predictions for the structure functions and cross-section calculations. Their predictions are tuned to include mostly s-wave and very little p-wave contribution very close to threshold at high Q^2. This also explains the good agreement of the extracted E_{0+} and $G_1^{\pi^0 p}$ to their predictions but the strong disagreement of the S_{0+}, $G_2^{\pi^0 p}$, the cross sections, and the structure functions.

The extracted generalized form factors, $G_1^{\pi^0 p}$ and $G_2^{\pi^0 p}$, show a faster falloff than the dipole form. This suggests a broadening of the spatial distribution of the correlated pion-nucleon system. It suggests that the correlated pion-nucleon system is broader than the bare nucleon itself because the bare nucleon follows the dipole form factor.

The results for $G_1^{\pi^0 p}$ show similar trends to the previously extracted $G_1^{\pi^+ n}$ [15]. In comparison, the former is about 30% higher in magnitude while the overall behavior as a function of Q^2 is similar. There are no results for $G_2^{\pi^+ n}$ for comparison. However, the generalized form factor results for the $\pi^0 p$ channel provide strong constraints on chiral aspects of the nucleon structure and the validity of the LETs at high Q^2.

ACKNOWLEDGMENTS

The authors thank Vladimir Braun for insightful discussions on the theoretical aspects of this work. The authors also acknowledge the excellent efforts of the Jefferson Lab's Accelerator and the Physics Divisions for making this experiment possible. This work was supported in part by the US National Science Foundation, the US Department of Energy, the Italian Istituto Nazionale di Fisica Nucleare, the French Centre National de la Recherche Scientifique, the French Commissariat à l'Énergie Atomique, the United Kingdom's Science and Technology Facilities Council, the Chilean Comisión Nacional de Investigación Científica y Tecnológica, the Scottish Universities Physics Alliance, and the National Research Foundation of Korea. The Southeastern Universities Research Association (SURA) operated the Thomas Jefferson National Accelerator Facility for the US Department of Energy under Contract No. DE-AC05-84ER40150.

[1] N. M. Kroll and M. A. Ruderman, Phys. Rev. **93**, 233 (1954).
[2] D. Drechsel and L. Tiator, J. Phys. G **18**, 449 (1992).
[3] Y. Nambu and D. Lurié, Phys. Rev. **125**, 1429 (1962).
[4] Y. Nambu and E. Shrauner, Phys. Rev. **128**, 862 (1962).
[5] R. Beck *et al.*, Phys. Rev. Lett. **65**, 1841 (1990).
[6] A. I. Vainshtein and V. I. Zakharov, Nucl. Phys. B **36**, 589 (1972).
[7] S. Scherer and J. H. Koch, Nucl. Phys. A **534**, 461 (1991).
[8] T. P. Welch *et al.*, Phys. Rev. Lett. **69**, 2761 (1992).
[9] For convenience, we use units where $c = \hbar = 1$ throughout the document unless noted otherwise.
[10] P. V. Pobylitsa, M. V. Polyakov, and M. Strikman, Phys. Rev. Lett. **87**, 022001 (2001).
[11] A. V. Efremov and A. V. Radyushkin, Phys. Lett. B **94**, 245 (1980).
[12] G. P. Lepage and S. J. Brodsky, Phys. Rev. D **22**, 2157 (1980).
[13] V. M. Braun, D. Y. Ivanov, A. Lenz, and A. Peters, Phys. Rev. D **75**, 014021 (2007).
[14] V. M. Braun, D. Y. Ivanov, and A. Peters, Phys. Rev. D **77**, 034016 (2008).
[15] K. Park *et al.*, Phys. Rev. C **85**, 035208 (2012).
[16] E. Amaldi, S. Fubini, and G. Furlan, *Pion-Electroproduction* (Springer-Verlag, New York, 1979).
[17] B. A. Mecking *et al.*, Nucl. Instrum. Methods Phys. Res., Sect. A **503**, 513 (2003).
[18] M. D. Mestayer *et al.*, Nucl. Instrum. Methods Phys. Res., Sect. A **449**, 81 (2000).
[19] E. S. Smith *et al.*, Nucl. Instrum. Methods Phys. Res., Sect. A **432**, 265 (1999).
[20] G. Adams *et al.*, Nucl. Instrum. Methods Phys. Res., Sect. A **465**, 414 (2001).

[21] M. Amarian *et al*., Nucl. Instrum. Methods Phys. Res., Sect. A **460**, 239 (2001).
[22] J. Alcorn *et al*., Nucl. Instrum. Methods Phys. Res., Sect. A **522**, 294 (2004).
[23] J. Beringer *et al*., Phys. Rev. D **86**, 010001 (2012).
[24] M. Ungaro *et al*., Phys. Rev. Lett. **97**, 112003 (2006).
[25] K. Park *et al*., Phys. Rev. C **77**, 015208 (2008).
[26] L. I. Schiff, Phys. Rev. **87**, 750 (1952).
[27] R. Ent, B. W. Filippone, N. C. R. Makins, R. G. Milner, T. G. O'Neill, and D. A. Wasson, Phys. Rev. C **64**, 054610 (2001).
[28] D. Drechsel, S. S. Kamalov, and L. Tiator, Eur. Phys. J. A **34**, 69 (2007).
[29] A. Villano *et al*., Phys. Rev. C **80**, 035203 (2009).
[30] A. Afanasev, I. Akushevich, V. Burkert, and K. Joo, Phys. Rev. D **66**, 074004 (2002).
[31] P. E. Bosted, Phys. Rev. C **51**, 409 (1995).
[32] I. G. Aznauryan *et al*., Phys. Rev. C **80**, 055203 (2009).
[33] I. Bedlinskiy *et al*., Phys. Rev. Lett. **109**, 112001 (2012).
[34] R. Arndt *et al*., Chin. Phys. C **33**, 1063 (2009).
[35] I. Aznauryan and V. Burkert, Prog. Part. Nucl. Phys. **67**, 1 (2012).
[36] K. M. Watson, Phys. Rev. **95**, 228 (1954).